An efficient and earth-abundant oxygen-evolving electrocatalyst based on amorphous metal borides

Nsanzimana, Jean Marie Vianney; Peng, Yuecheng; Xu, Yang Yang; Thia, Larissa; Wang, Cheng; Xia, Bao Yu; Wang, Xin

2017

Nsanzimana, J. M. V., Peng, Y., Xu, Y. Y., Thia, L., Wang, C., Xia, B. Y., & Wang, X. (2018). An efficient and earth-abundant oxygen-evolving electrocatalyst based on amorphous metal borides. Advanced Energy Materials, 8(1), 1701475-. doi:10.1002/aenm.201701475

https://hdl.handle.net/10356/106687

https://doi.org/10.1002/aenm.201701475

Article type: Full Paper

An Efficient and Earth-Abundant Oxygen-Evolving Electrocatalyst Based on Amorphous Metal Borides

Jean Marie Vianney Nsanzimana,[a] Yuecheng Peng,[a] Yang Yang Xu,[b] Larissa Thia,[a] Cheng Wang, [c] Bao Yu Xia,[b] and Xin Wang [a]**

J. M. V. Nsanzimana, Y. Peng, Dr. L. Thia, Prof. X. Wang
School of Chemical and Biomedical Engineering - Nanyang Technological University, 50 Nanyang Avenue, Singapore 639798, Singapore
E-mail: Wangxin@ntu.edu.sg
Y. Y. Xu, Prof. B. Y. Xia
Key Laboratory of Material Chemistry for Energy Conversion and Storage, Ministry of Education, Hubei, Key Laboratory of Material Chemistry and Service Failure, School of Chemistry and Chemical Engineering, Wuhan National Laboratory for Optoelectronics, Huazhong University of Science and Technology, 1037 Luoyu Road, Wuhan, 430074, China
E-mail: byxia@hust.edu.cn
C. Wang
Institute for New Energy Materials & Low-Carbon Technologies, Tianjin University of Technology, Tianjin, P.R. China.

Keywords: Oxygen evolution, Electrocatalyst, Metal boride, Amorphous structure, Electronic effect

Cost-effective and efficient oxygen-evolving electrocatalysts are urgently required for energy storage and conversion technologies. In this work, an amorphous trimetallic boride nanocatalyst (Fe-Co-2.3Ni-B) prepared by a simple approach is reported as a highly efficient OER electrocatalyst. It exhibits an overpotential (η) of 274 mV to deliver a geometric current density (j_{geo}) of 10 mA cm^{-2}, a small Tafel slope of 38 mV dec^{-1}, and excellent long-term durability at a mass loading of 0.3 mg cm^{-2}. The impressive electrocatalytic performance originates from the unique amorphous multimetal-metalloid complex nanostructure. From application point of view, this work holds great promise as this process is simple and allows for large scale production of cheap yet efficient material.

1. Introduction

Electrochemical energy technologies, including rechargeable metal-air batteries, regenerative fuel cells, and water coupled carbon dioxides conversion have aroused a great interest as attractive alternatives for clean and efficient energy production.[1] These devices involve oxygen evolution reaction (OER) at the anodic electrodes which is a thermodynamic up-hill reaction and exhibits sluggish kinetics coupled with multiple electrons and protons, and thus it contributes significantly to the efficiency loss of the overall electrochemical process.[2] Therefore, efficient OER electrocatalyst is a cornerstone for the sustainable energy storage and conversion technologies.[3] Noble metal-based catalysts such as Ru and Ir oxides have been reported to be excellent OER catalysts,[4] however, their low natural abundance and higher-cost render their widespread commercial utilisation impractical.[5] Thus, developing efficient, durable and cost-effective catalytic materials for OER is crucial, but so far still remains a great challenge.

Recently, various metal-metalloid compound materials such as chalcogenides, nitrides, and phosphides have been reported to exhibit promising OER electrocatalytic activities.[6] This has been attributed to the charge transfer between different elements and the modified electronic structures, and consequently lower the kinetic energy barriers of the electrochemical processes.[7] In this regard, to extend such applications on metal borides is reasonable, wherein metal borides shares certain properties with other metal-metalloid such as bonding schema in metal phosphides.[8] Recently, the application of monometallic borides such as cobalt boride, iron boride, and nickel boride as well as cobalt borate-based graphene hybride as oxygen-evolving catalyst have been reported to exhibit promising electrocatalytic activity for OER in alkaline media.[9] However, multimetal-metalloid boron-based material herein refered as an amorphous quaternary metal borides for simplicity as oxygen-evolving electrocatalyst reported to date is very limited. Thus, it is still of great interest to develop metal boride-based OER catalysts and further explore their catalytic activity. The as-identified

approach to enhance electrochemical OER properties in metal-metalloid material open a new avenue in related applications for energy devices that involves OER such as water electrolysis and metal-air batteries.

Despite of complicated structure of amorphous material, well-characterized amorphous nanomaterial as oxygen-evolving material have received attention due to the unique properties such as higher catalytic selectivity and activity.[10] A great number of under-coordinated metal atoms, and hence abundant defects, in amorphous nanomaterial may provide more reactive sites at the catalyst surface, and as a result facilitating binding of hydroxyls and thus enhancing OER performance.[11] Furthermore, these amorphous nanomaterials have attracted much attention in other electrochemical application such as in pseudo-capacitors, Li-ion batteries, sensor and water oxidation.[12] In some studies, it was found that amorphous multimetal oxygen-evolving material exhibited higher electrochemical performance than corresponding crystalline material when annealed.[13] Herein we report an amorphous quaternary metal-boron based catalyst (designated as Fe–Co–2.3Ni–B) with a higher OER electrocatalytic activity than commercial Ir/C (20 wt %) catalyst. The incorporation of more metals has been found to be an effective strategy to tune the catalytic activity of metal-metalloid catalyst *via* charge transfer.[8] This study not only provides the effective metal boride electrocatalysts, but also elucidates the effective approach to boost the OER electrocatalytic property of the metal-boron based materials, and thus promote such materials to the energy applications in OER-related systems.

2. Results and Discussion

The metal boride materials are prepared by the reduction of metal precursors in the presence of sodium borohydride ($NaBH_4$), followed by drying at 45 °C for overnight under argon atmosphere. Here, $NaBH_4$ acts as not only the reducing agent but also the boron precursor, and additionally, as the stabilizing element during chemical reaction and as a result an amorphous product is expected.[14] **Figure 1**a shows the polydispersed nanoparticles in a

typical field-emission scanning electron microscopy (FESEM) image of the as-prepared Fe–Co–2.3Ni–B product. The size of Fe–Co–2.3Ni–B nanoparticles vary approximately in 30 ~ 40 nm, as observed in transmission electron microscopy (TEM) image (Figure 1b). An extension of amorphous layer revealed in Figure 1b can be observed clearly in Figure 1c, which is proposed as a thin metal oxide/borates layer on metal borides particles.[9a] The inset of Figure 1c shows selected area electron diffraction (SAED) pattern with no dots or distinct rings, which indicates amorphous structure. The absence of sharp crystalline peak and the appearance of single broad peak at approximately 45° in Figure 1d obviously reveals that the as-synthetized trimetallic boride is amorphous, which is in agreement with SAED result. The ternary metal-boron catalyst (designated as Fe–2.3Ni–B and Co–2.3Ni–B) also show the similar amorphous phase (Figure S1, Supporting Information). The XRD observation for amorphous boron-based material was used to differentiate the predominance of either metal borides which exhibits the diffraction in the 2θ range between 40 and 50, or 30 and 40° for boron oxides species predominance.[15] Obviously, the absence of a shoulder broad peak for the amorphous boron oxides in low diffraction 2θ range indicates the formation of metal borides.[15-16]

The analysis of SEM image and corresponding energy dispersive X-ray (EDX) spectroscopy elemental mappings of the amorphous quaternary Fe–Co–2.3Ni–B nanoparticles clearly demonstrates the homogenous distribution of Fe, Co, Ni and B (Figure S2, Supporting Information). After the electrochemical test, the oxygen atomic percentage of product is at 3.7 %, which would be attributed to the partial oxidation on the catalyst surface (Figure S3 and Table S1, Supporting Information). It is clear that the peak appears at ~1.52 V (V vs. RHE) in the first scan and maintains at ~1.45 V in the following cycles (Figure S4, Supporting Information). This is associated to the formation of oxidized species, and the growth of the surface oxide/hydroxide layer would serve as the catalytic sites for O_2-evolving process,[9a] which is similar to the identified oxide and/or hydroxide thin layer on the catalyst

core as the catalytic site for metal phosphide based oxygen-evolving catalysts in alkaline solution.[6b, 9a, 17]

The surface chemistry and electronic structure of the as-prepared material are studied by X-ray photoelectron spectroscopy (XPS, Figure S5a, Supporting Information. All spectra in constituent elements are calibrated to C 1s at 254.5 eV (Figure S5b, Supporting Information). The B 1s spectrum in the amorphous Fe–Co–2.3Ni–B nanoparticles show a peak at 188.2 eV (**Figure 2**a), corresponding to boron in metal borides which is in agreement with previous literature.[9a] Positive chemical shift of 0.8 eV for B compared to pure B is observed.[18] The formation of borides is attributed to the interactions of B with metals through the electron transfer occupying vacant *d*-orbitals of metal, and hybridization of B 2p states with the metal *d*-orbitals.[19] The peak around Ni $2p_{3/2}$ spectrum in Figure 2b at low-binding energy of 852.6 eV corresponds to the Ni in nickel boride which is in agreement with literature on nickel boride.[9b] Constistently, Co $2p_{3/2}$ spectrum in Figure 2c shows a major peak at 778.2 eV which is attributed to the interaction of Co with boron in cobalt boride, while the peak at 707.1 eV is ascribed to Fe in iron boride (Figure 2d). The peaks of oxidized species in metal borides are inadvertently formed due to the exposure to the atmosphere.[9a] Recently, the effect of exposure of nickel boride to air for significant time was clearly explored and oxidized species were in predominance.[9b] The electron transfer nature between the constituent elements noticed by the binding energy shifts in B 1s spectrum makes boron electron deficient while metals are enriched with electron, may makes the electron transfer favorable during the sluggish multistep OER process.

The OER electrocatalytic activities of the as-prepared materials are investigated in 1.0 M KOH solution. The anodic current density of quaternary Fe–Co–2.3Ni–B nanoparticle shows an onset potential of 1.46 V (at j_{geo} = 1.0 mA cm^{-2}), while it is at 1.49 V for commercial Ir/C catalyst (**Figure 3**a). Furthermore, it requires a η of 274 mV to afford a j_{geo} of 10 mA cm^{-2}, while commercial Ir/C catalyst requires 317 mV. Additionally, Tafel slope of 38 mV dec^{-1} is

even smaller than that of Ir/C catalyst, 54 mV dec^{-1} (Figure 3b), and hence, it implies more favorable OER kinetics for the as-prepared quaternary metal boride.[20] Figure 3c clearly reveals that iron-based boron material is less active than Co- and Ni-based binary metal-boron catalyst. Interestingly, the incorporation of Fe into Ni–B catalyst to form ternary material outperforms the incorporation of Co (Figure S6, Supporting Information), whereby 294 and 317 mV are overpotentials required to derive a j_{geo} of 10 mA cm^{-2} for Fe–2.3Ni–B and Co–2.3Ni–B nanoparticles, respectively. Obviously, the presence of Fe is crucial for high-performance of OER composite catalysts.[21] Furthermore, a maximum improvement in OER performance is demonstrated when both Fe and Co are incorporated to form trimetallic boride (Fe-Co–2.3Ni–B) (Figure 3c, Table S2, Supporting Information). Electrochemical impedance spectroscopy was further used to characterize the OER kinetics .[22] The reduced semicircular diameter in Nyquist plots compared to ternary ones and commercial Ir/C catalysts (Figure S7, SI) reveals charge-transfer resistance reduction when both Co and Fe are incorporated in the nanoparticles.[20, 23]

We investigated the electrochemical double-layer capacitance which is proportional to the electrochemically active surface area (ECSA).[17a, 24] As can be seen, the measured capacitance for quaternary Fe–Co–2.3Ni–B nanoparticles is 0.17 mF cm^{-2}, which is roughly twice of monometallic Ni–B nanoparticles (Figure S8, Supporting Information). Additionally, the derived ECSA from capacitance is 4.25 cm^2 and 2.5 cm^2 for trimetallic and monometallic nanopartcles, respectively, and thus indicating an enhanced electrocatalytic active site density. Furthermore,the specific activity defined as the specific current density per catalyst surface area (j_s) is further calculated.[24a] The specific current density per catalyst surface area (j_s) at η = 0.314 V is calculated from the measured double layer capacitance by using general specific capacitances of Cs = 0.040 mF cm^{-2} in 1 M NaOH based on typical reported values,[24a, 25] and it is 4.1 mA cm^{-2} and 0.7 mA cm^{-2} for the as-prepared amorphous metal boride and monometallic nickel boride, respectively. This observation is in agreement with the reduced η

required to afford a j_{eo} of 10 mA cm^{-2} by 40 mV, and the reduction of Tafel slope Ni–B nanoparticles from 52 to 38 mV dec^{-1} for quaternary metal boride at the same loading (Figure S6, and Table S2, Supporting Information). Hence, this supports the enhancement of specific catalytic activity through the incorporation of Co and Fe compared to monometallic nickel boron-based nanoparticles. For multimetal based OER electrocatalyst, it has been suggested that the thermodynamic barrier of a proton-coupled electron transfer (PCET) pre-equilibrium could be reduced while facilitating O−O bond formation by adding other metal in monometallic based catalyst, and thus, leading to an enhanced catalytic activity.[7b]

The optimization of the catalyst is studied by varying the ratios of Fe and Co precursors during the preparation of trimetallic boride, and it reveals that their incorporation have a significant influence on tuning the OER activity of trimetallic boride nanoparticles (Figure 3d, and Figure S11, Supporting Information). This is attributed to general mechanism of metal-metalloid catalyst, where the transition metal cations on the surface undergo oxidation to MOOH surrounding the catalyst core (where, M = Fe, Co, and Ni),[9b, 25a] and may serve as the actual multimetal surface-active sites in multimetal oxides-based O_2-evolving catalyst.[17a, 26] To extend the viability of this technique to synthetise oxygen-evolving trimetallic boride, another iron precursor in aqueous solution which contain iron (II) is investigated and the catalytic activity is merely similar. It requires 1.513 V to reach a j_{geo} of 10 mA cm^2, which is only higher than the as-prepared Fe–Co–2.3Ni–B nanoparticles by 9 mV (Figure S12, Supporting Information). The as-prepared trimetallic boride material is comparable and/or even more efficient than the other nickel, cobalt and/or iron metal-metalloids, metal oxyphosphides and oxides catalyst for electrochemical OER application in literatures reported (Table S3, Supporting Information). And thus, as an earth abundant based catalyst prepared by simple approach, further studies can be carried out to the other multimetal-boron based material.

Additionally, we further prepared iron-cobalt-nickel alloy with a similar metal precursor

ratio in the mother solution, and it's OER performance is lower than that of the amorphous quaternary Fe–Co–2.3Ni–B catalyst (Figure S13, Supporting Information). It requires an η of 323 mV to achieve a a j_{geo} of 10 mV cm^{-2}, which is 49 mV more compared to quaternary metal boride in the similar testing condition and loading. The poor performance of this metal alloy may prove that B in amorphous metal boride contributes to electronic structure and hence, enhance charge density distribution in metal boride alloy which facilitates the balance of chemisorption and desorption of reaction intermediates.[25a, 27] This is the case for other metal-metalloid such as P, N, and Se, whereby it is suggested that these non-metallics bear an intrinsic role in enhancing the activity of metal by in-situ formation of metal hydroxide active sites, while other authors attributes to the synergistic effects between metal with non-metal elements but not yet fully explained.[17a, 28] The enhanced electrocatalytic activity of the as-prepared quaternary metal borides may be attributed to the (1) improved active surface area compared to the monometallic nickel boride material, and (2) enhanced electron transfer due to the unique amorphous multimetal-metalloid complex nanostructure capable of buffering multistep OER process in harsh alkaline electrolytes.

The stability of oxygen-evolving catalyst is crucial for energy storage and conversion technologies. Hence, the galvanostatic test investigated at a constant current density of 10 mA cm^{-2} at room temperature in 1.0 M alkaline electrolyte shows a nearly constant η for amorphous quaternary metal-boron nanoparticles over a period of 12 h (**Figure 4**a). Furthermore, both ternary metal-boron exhibits promising stability, whereby Co–2.3Ni–B catalyst shows an improved activity after one hour of stability test and maintains the activity over time, while Fe–2.3Ni–B catalyst shows merely no significant potential loss over the whole test period (Figure S14, Supporting Information). To support the galvanostatic results, the cycle capability of the material is tested. The initial and the *i*R-corrected LSV curves recorded after 1000 cycles also show the promising stability (Figure 4b), while similar trend is

observed in ternary metal-borides (Figure S15, Supporting Information). Furthermore, SEM images for amorphous trimetallic boride show no morphology change after long-term galvanostatic operation (Figure S16, Supporting Information). In addition, from the metal-metalloid interaction perspective, the stability is predictable as there is a higher covalency of metal-boron bond which is even higher than metal-phosphorous bond which makes them extremely hard and chemically resistant.[8] Though, precious metal-based electrodeposited IrO_x catalyst showed comparable OER activity for the as-prepared material, in which it affords 10 mA cm^{-2} current density at $\eta = 0.32 \pm 0.04$ V, it was unstable during 2 h of constant current electrolysis in alkaline electrolytes.[24a] In contrast, the long-term durability indicates that this non-precious metal catalyst derivatives can survive the harsh alkaline electrolytes but not the precious metal-based catalysts.

Finally, a two-electrode electrolyzer using a modified carbon fiber paper (CFP) by Fe–Co–2.3Ni–B nanoparticles (denoted as Fe–Co–2.3Ni–B/CFP) and 50% Pt/C catalyst (denoted as 50% Pt/C /CFP) is demonstrated to drive the practical water splitting in 1.0 M KOH solution. Figure 4c shows that a low voltage of 1.52 V is required to afford a current density of 20 mA cm^{-2}, and the whole electrolysis is fairly stable during the 24 h operation (Figure 4d). Additionally, though we herein report a highly efficient amorphous quaternary metal boride for OER, results also reveals that this material can work for overall water splitting as both anode and cathode (Figure S17, Supporting Information). It requires a voltage of 1.66 V to deliver a current density of 10 mA cm^{-2} and it also exhibits outstanding stability over a period of 10 h.

3. Conclusion

In summary, an amorphous quaternary metal-boron based material is synthesized by an economically viable approach. The as-prepared Fe–Co–2.3Ni–B nanocatalyst demonstrates an excellent electrocatalytic activity towards OER. The oxygen-evolving activity of trimetallic

boride is associated with oxides/hydroxides metals layer which serves as the catalytically active site in alkaline electrolyte, while B assists by electron transfer. For application purposes, this material requires only 1.52 V to achieve 20 mA cm^{-2} (j_{geo}) when is used as anodic material during overall water splitting in 1.0 M KOH electrolyte. Overall, this study not only provides an earth-abundant and efficient oxygen-evolving electrocatalyst, but also it opens up an avenue to explore the efficient and low-cost metal boride catalyst for energy technologies related to OER.

Supporting Information

Supporting Information is available from the Wiley Online Library or from the author.

Acknowledgements

This project is funded by the National Research Foundation (NRF), Prime Minister's Office, Singapore under its Campus for Research Excellence and Technological Enterprise (CREATE) programme. We also acknowledge financial support from Startup grant (M4081887), College of Engineering, Nanyang Technological University, and the academic research fund AcRF tier 2 (M4020246, ARC10/15), Ministry of Education, Singapore. The financial support by the Innovation Foundation of Shenzhen Government (JCYJ20160408173202143), the Joint Fund of Energy Storage of Qingdao (20160012) and the Fundamental Research Funds of Huazhong University of Science and Technology (3004013109, 0118013089) is also acknowledged.

References

[1] a) N. Armaroli, V. Balzani, *Angew. Chem. Int. Ed.* **2007**, *46*, 52; b) R. Schlögl, *ChemSusChem* **2010**, *3*, 209.
[2] J. Greeley, N. M. Markovic, *Energy Environ. Sci.* **2012**, *5*, 9246.
[3] I. Katsounaros, S. Cherevko, A. R. Zeradjanin, K. J. Mayrhofer, *Angew. Chem. Int. Ed.* **2014**, *53*, 102.
[4] a) T. Reier, M. Oezaslan, P. Strasser, *ACS Catal.* **2012**, *2*, 1765; b) P. Lettenmeier, L. Wang, U. Golla-Schindler, P. Gazdzicki, N. A. Cañas, M. Handl, R. Hiesgen, S. S. Hosseiny, A. S. Gago, K. A. Friedrich, *Angew. Chem. Int. Ed.* **2016**, *55*, 742.

[5] a) S. Floquet, M. E. G. Lyons, *Phys. Chem. Chem. Phys.* **2011**, *13*, 5314; b) T. R. Cook, D. K. Dogutan, S. Y. Reece, Y. Surendranath, T. S. Teets, D. G. Nocera, *Chem. Rev.* **2010**, *110*, 6474.

[6] a) G.-F. Chen, T. Y. Ma, Z.-Q. Liu, N. Li, Y.-Z. Su, K. Davey, S.-Z. Qiao, *Adv. Funct. Mater.* **2016**, *26*, 3314; b) B. Y. Guan, L. Yu, X. W. Lou, *Angew. Chem. Int. Ed.* **2017**, *129*, 2426; c) D. Li, H. Baydoun, B. Kulikowski, S. L. Brock, *Chem. Mater.* **2017**, *29*, 3048.

[7] a) A. Mendoza-Garcia, H. Zhu, Y. Yu, Q. Li, L. Zhou, D. Su, M. J. Kramer, S. Sun, *angew. Chem. Int. Ed.* **2015**, *54*, 9642; b) D. Li, H. Baydoun, C. N. Verani, S. L. Brock, *J. Am. Chem. Soc.* **2016**, *138*, 4006.

[8] S. Carenco, D. Portehault, C. Boissière, N. Mézailles, C. Sanchez, *Chem. Rev.* **2013**, *113*, 7981.

[9] a) J. Masa, P. Weide, D. Peeters, I. Sinev, W. Xia, Z. Sun, C. Somsen, M. Muhler, W. Schuhmann, *Adv. Energy Mater.* **2016**, *6*, 1502313; b) J. Masa, I. Sinev, H. Mistry, E. Ventosa, M. de la Mata, J. Arbiol, M. Muhler, B. Roldan Cuenya, W. Schuhmann, *Adv. Energy Mater.* **2017**, 1700381; c) W.-J. Jiang, S. Niu, T. Tang, Q.-H. Zhang, X.-Z. Liu, Y. Zhang, Y.-Y. Chen, J.-H. Li, L. Gu, L.-J. Wan, J.-S. Hu, *Angew. Chem. Int. Ed.* **2017**, *56*, 6572; d) P. Chen, K. Xu, T. Zhou, Y. Tong, J. Wu, H. Cheng, X. Lu, H. Ding, C. Wu, Y. Xie, *Angew. Chem. Int. Ed.* **2016**, *55*, 2488.

[10] J. Nai, H. Yin, T. You, L. Zheng, J. Zhang, P. Wang, Z. Jin, Y. Tian, J. Liu, Z. Tang, L. Guo, *Adv. Energy Mater.* **2015**, *5*, 1401880.

[11] Y. Yang, F. Huilong, R. Gedeng, X. Changsheng, M. T. James, *ACS nano* **2014**, *8*, 9518.

[12] a) F. Tian, M. Radin, D. Siegel, *Chem. Mater.* **2014**, *26*, 2952; b) L. Kuai, J. Geng, C. Chen, E. Kan, Y. Liu, Q. Wang, B. Geng, *Angew. Chem. Int. Ed.* **2014**, *53*, 7547.

[13] P. Liu, S. Yang, L. Zheng, B. Zhang, H. Yang, *Chem. Sci.* **2017**, *8*, 3484.

[14] J. Vanwonterghem, S. Morup, C. J. W. Koch, S. W. Charles, S. Wells, *Nature* **1986**, *322*, 622.

[15] G. M. Arzac, T. C. Rojas, A. Fernandez, A. Fernández, *ChemCatChem* **2011**, *3*, 1305.

[16] P. Kukula, V. Gabova, K. Koprivova, P. Trtik, *Catal. Today* **2007**, *121*, 27.

[17] a) P. He, X. Y. Yu, X. W. Lou, *Angew. Chem. Int. Ed.* **2017**, *56*, 3897; b) Y. Yan, B. Y. Xia, X. Ge, Z. Liu, A. Fisher, X. Wang, *Chem. – Eur. J.* **2015**, *21*, 18062; c) L.-A. Stern, L. Feng, F. Song, X. Hu, *Energy Environ. Sci.* **2015**, *8*, 2347.

[18] J. F. Moulder, J. Chastain, R. C. King, *Handbook of X-ray Photoelectron Spectroscopy : a Reference Book of Standard Spectra for Identification and Interpretation of XPS data, Eden Prairie, Minn. : Physical Electronics, c1995* **1995**.

[19] Y. Okamoto, Y. Nitta, T. Imanaka, S. Teranishi, *J. Chem. Soc., Faraday Trans. 1* **1979**, *75*, 2027.

[20] E. Fabbri, A. Habereder, K. Waltar, R. Kotz, T. J. Schmidt, *Catal. Sci. Tech.* **2014**, *4*, 3800.

[21] D. Friebel, M. W. Louie, M. Bajdich, K. E. Sanwald, Y. Cai, A. M. Wise, M.-J. Cheng, D. Sokaras, T.-C. Weng, R. Alonso-Mori, R. C. Davis, J. R. Bargar, J. K. Nørskov, A. Nilsson, A. T. Bell, *J. Am. Chem. Soc.* **2015**, *137*, 1305.

[22] Y. Pi, Q. Shao, P. Wang, F. Lv, S. Guo, J. Guo, X. Huang, *Angew. Chem. Int. Ed.* **2017**, *56*, 4502.

[23] S. Giménez, J. Bisquert, *J. Photoelectrochemical Solar Fuel Production : From Basic Principles To Advanced Devices. Switzerland : Springer* **2016**.

[24] a) C. C. L. McCrory, S. Jung, J. C. Peters, T. F. Jaramillo, *J. Am. Chem. Soc.* **2013**, *135*, 16977; b) Y. Wang, Y. Zhang, Z. Liu, C. Xie, S. Feng, D. Liu, M. Shao, S. Wang, *Angew. Chem. Int. Ed.* **2017**, *56*, 5867.

[25] a) H. Li, P. Wen, Q. Li, C. Dun, J. Xing, C. Lu, S. Adhikari, L. Jiang, D. L. Carroll, S. M. Geyer, *Adv. Energy Mater.*, 1700513; b) J. Zhang, Y. Hu, D. Liu, Y. Yu, B. Zhang, *Adv. Sci.* **2017**, *4*, 1600343; c) C. Zhang, Y. Huang, Y. Yu, J. Zhang, S. Zhuo, B. Zhang, *Chem Sci* **2017**, *8*, 2769.

[26] a) R. Liu, Y. Wang, D. Liu, Y. Zou, S. Wang, *Adv. Mater.* **2017**, 1701546; b) B. Zhang, X. Zheng, O. Voznyy, R. Comin, M. Bajdich, M. García-Melchor, L. Han, J. Xu, M. Liu, L. Zheng, F. P. García de Arquer, C. T. Dinh, F. Fan, M. Yuan, E. Yassitepe, N. Chen, T. Regier, P. Liu, Y. Li, P. De Luna, A. Janmohamed, H. L. Xin, H. Yang, A. Vojvodic, E. H. Sargent, *Science* **2016**, *352*, 333; c) M. Gorlin, J. F. de Araujo, H. Schmies, D. Bernsmeier, S. Dresp, M. Gliech, Z. Jusys, P. Chernev, R. Kraehnert, H. Dau, P. Strasser, *J. Am. Chem. Soc.* **2017**, *139*, 2070.

[27] a) S. Gupta, N. Patel, A. Miotello, D. C. Kothari, *J. Power Sources* **2015**, *279*, 620; b) P. Zhang, M. Wang, Y. Yang, T. Yao, H. Han, L. Sun, *Nano Energy* **2016**, *19*, 98.

[28] C. Tang, N. Cheng, Z. Pu, W. Xing, X. Sun, *Angew. Chem. Int. Ed.* **2015**, *54*, 9351.

Figures and captions

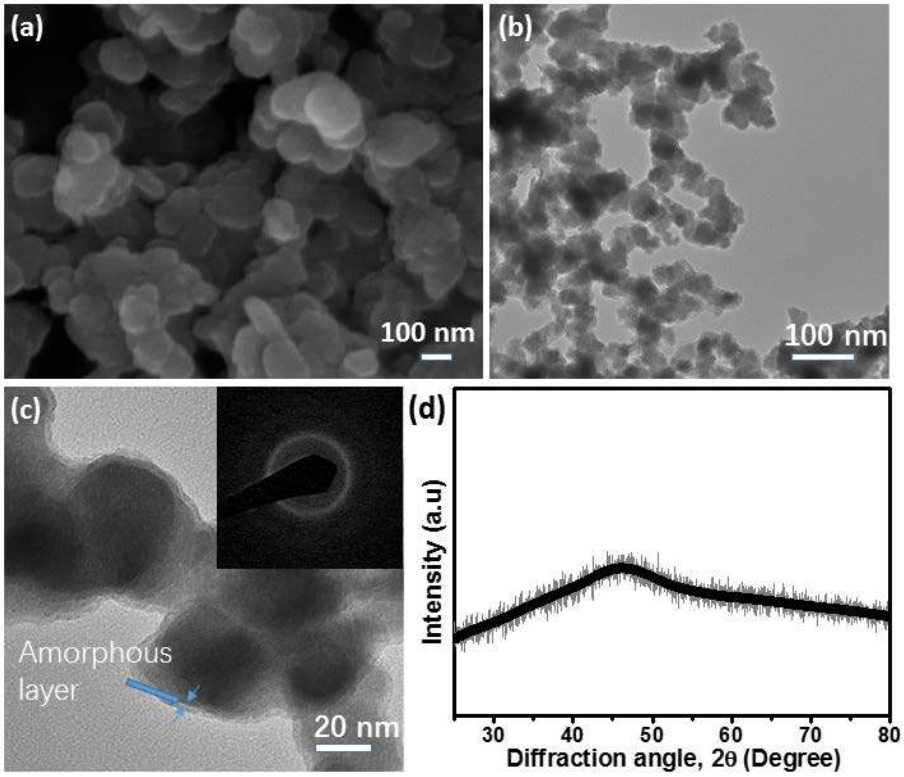

Figure 1. a) SEM, (b) and (c) TEM images, the SAED pattern in inset Figure 1c, (d) XRD pattern of amorphous quaternary Fe–Co–2.3Ni–B powders.

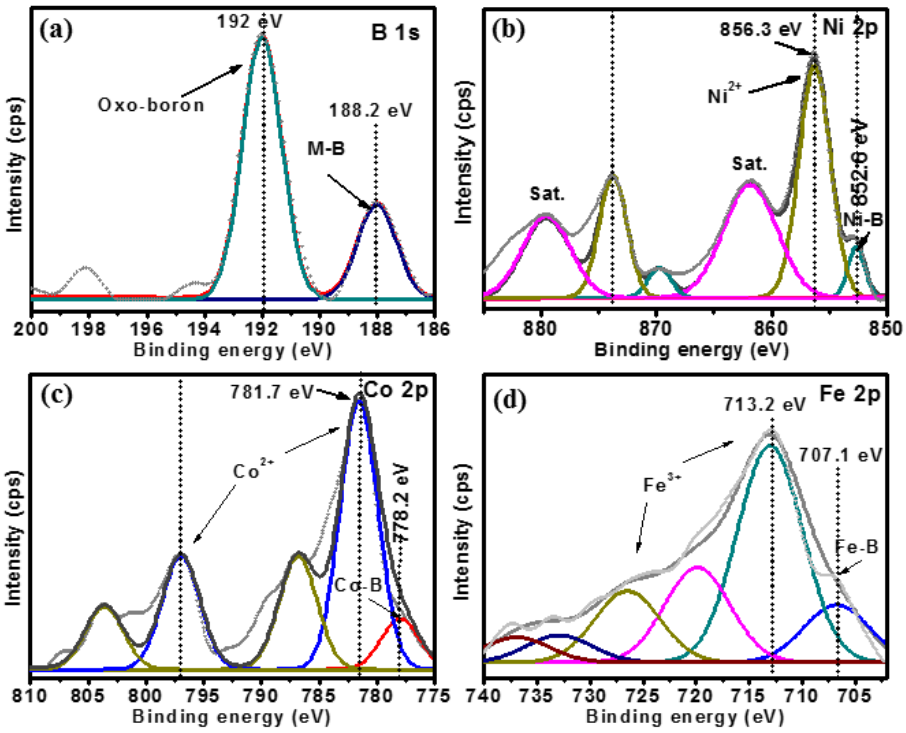

Figure 2. a) High-resolution XPS spectra of B 1s, (b) Ni 2p, (c) Co 2p, and (d) Fe 2p for amorphous quaternary Fe–Co–2.3Ni–B powders exposed to air after drying in Ar atmosphere for overnight.

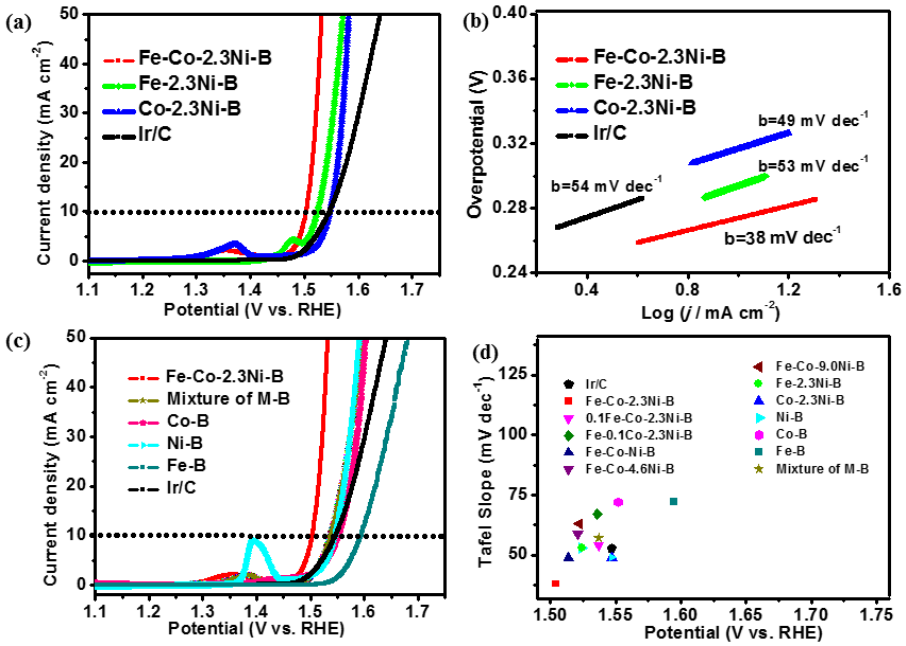

Figure 3. Electrochemical study of the as-synthesized metal borides and commercial 20 % Ir/C catalyst. a) *i*R-corrected LSV curves for quaternary, ternary metal-boron catalyst, and (b) Corresponding Tafel slopes. c) *i*R-corrected LSV curves for quaternary, mixture of M–B and binary catalyst. d) Comparison of different metal-boron material and Ir/C catalysts by using two parameters: potential required to afford a j_{geo} of 10 mA cm^{-2} *vs.* Tafel slopes.

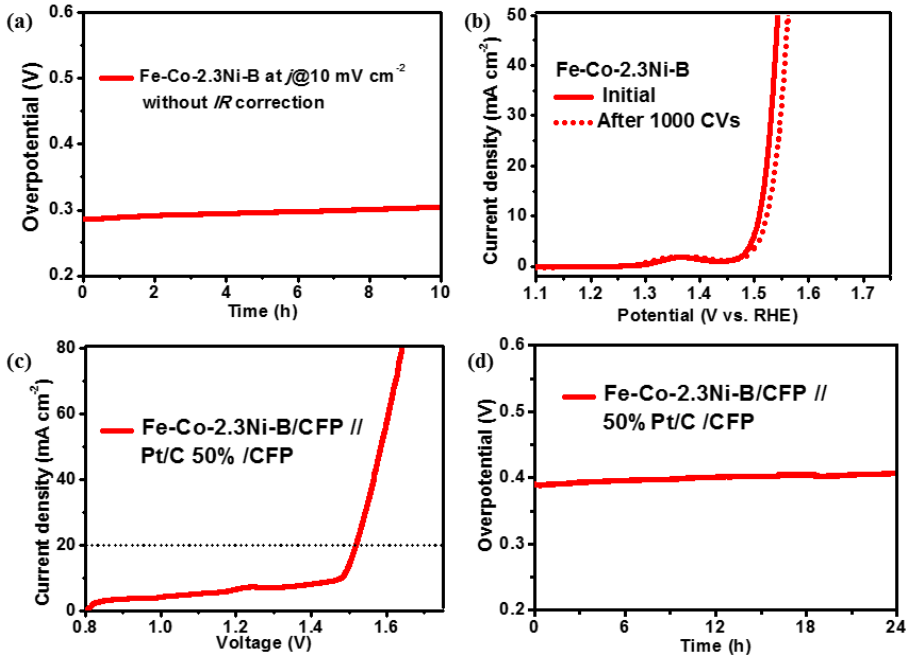

Figure 4. a) Galvanostatic long-term durability test of the as-prepared amorphous Fe–Co–2.3Ni–B nanocatalyst, (b) The electrochemical stability test. c) Current-potential response of a two-electrode alkaline electrolyzer, and (d) Galvanostatic electrolysis at 20 mA cm^{-2} over 24 h period. The loading of the active material is 4.0 mg cm^{-2}.

Table of Content

Amorphous trimetallic boride demonstrates an impressive electrocatalytic oxygen evolution activity, which originates from the tuned electronic properties of the constituent elements. Such earth-abundant boride electrocatalyst holds great promise for practical applications in water electro-splitting devices as the synthesis process is simple and allows for large scale production of cheap yet efficient material.

Keyword: Oxygen evolution, Electrocatalyst, Metal boride, Amorphous structure, Electronic effect

J. M. V. Nsanzimana,[a] Y. Peng,[a] Y. Yang Xu,[b] L. Thia,[a] C. Wang, [c] B. Y. Xia,[b]* and X. Wang [a]*

Title

An Efficient and Earth-Abundant Oxygen-Evolving Electrocatalyst Based on Amorphous Metal Borides

ToC figure

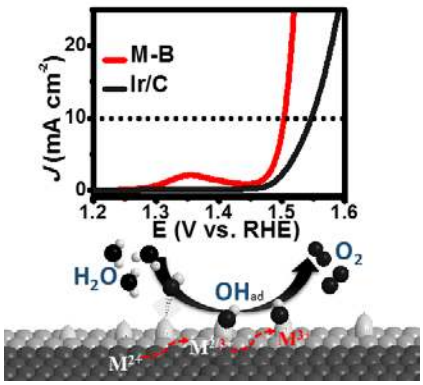

Supporting Information

An Efficient and Earth-Abundant Oxygen-Evolving Electrocatalyst Based on Amorphous Metal Borides

Jean Marie Vianney Nsanzimana,[a] Yuecheng Peng,[a] Yang Yang Xu,[b] Larissa Thia,[a] Cheng Wang, [c] Bao Yu Xia,[b] and Xin Wang [a]**

J. M. V. Nsanzimana, Y. Peng, Dr. L. Thia, Prof. X. Wang

School of Chemical and Biomedical Engineering - Nanyang Technological University, 50 Nanyang Avenue, Singapore 639798, Singapore

E-mail: Wangxin@ntu.edu.sg

Y. Y. Xu, Prof. B. Y. Xia

Key Laboratory of Material Chemistry for Energy Conversion and Storage, Ministry of Education, Hubei, Key Laboratory of Material Chemistry and Service Failure, School of Chemistry and Chemical Engineering, Wuhan National Laboratory for Optoelectronics, Huazhong University of Science and Technology, 1037 Luoyu Road, Wuhan, 430074, China

E-mail: byxia@hust.edu.cn

C. Wang

Institute for New Energy Materials & Low-Carbon Technologies, Tianjin University of Technology, Tianjin, China.

1. Materials Synthesis

The amorphous metal-boron based materials were prepared by reducing aqueous mixture containing metals precursor with a strong reducing agent, sodium borohydride ($NaBH_4$), which also acts as the boron source. The reduction of metal (M^{2+}) ions in an aqueous solution results into a precipitate of metal boride *via* the following reaction: $2MCl_2 + 4NaBH_4 + 9H_2O \rightarrow M_2B + 4NaCl + 12.5H_2 + 3B(OH)_3$ (equation 1).[1] However, there are parameters to control in order to ensure the occurrence of the reaction (1), as the final product depends on preparation conditions.[2] Thus, controlling BH_4^-/M ion ratio at three times, rapid mixing and anaerobic handling (during preparation and drying) are considered to ensure the formation of metal borides,[3] hence the as-prepared is refered as amorphous metal borides. The addition of reducing solution caused a lot of bubbles and the black precipitate was formed as a result of the reaction. The precipitates were washed subsequently with ultra-purified water and ethanol several times to remove excess ions and other undesired dissolved species such as Na^+, and Cl^- ions. The as-prepared black precipitates were collected by vacuum filtration, taken in a tubular reactor and dried overnight at 45 ◦C in an argon atmosphere to obtain the final stable black powders. All chemicals are used as received.

1.1 Synthesis of Binary Amorphous Metal Boride Powders

In a typical synthesis of binary metal boride (denoted as Co-B, Ni-B, and Fe-B), 10 mL of the precursor solution containing $CoCl_2$ (1.0 mmol, Sigma-Aldrich), $NiCl_2$ (1.0 mmol, Sigma-Aldrich), and $FeCl_2{\cdot}4H_2O$ (1.0 mmol, Sigma-Aldrich) were prepared in a three-neck flask, respectively. The reaction vessel was maintained at lower temperature by using water bath containing ice. The reducing solution containing $NaBH_4$ (Sigma-Aldrich) was also prepared in 0.1 M NaOH (Alfa Aesar), and afterward added to the metal precursor aqueous solution by a syringe in the argon gas atmosphere. The $NaBH_4$ solution being a strong reducing agent turned the aqueous solution black. The continuous vigorous mixing of this solution was maintained until the bubble stops. Then the precipitates were collected by centrifugation and washed subsequently with ultra-purified water and ethanol several times.

1.2 Synthesis of Amorphous Ternary and Quaternary Metal Boride Powders

The ternary and quaternary metal borides were prepared at the same conditions used in this study for monometallic boride catalyst. In a typical synthesis procedure of ternary metal-boron materials (denoted as Fe–2.3Ni–B and Co–2.3Ni–B, these ratio were used based on the fact that the highly quaternary metal boride was prepared in 1 : 1 : 2.3 for Fe : Co : Ni metal precursor in mother solution), a 10 mL precursor solution containing $NiCl_2$ (2.3 mmol) prepared in a three-neck flask was stirred about 30 minutes at lower temperature and in argon atmosphere. Simultaneously, proper amount of $CoCl_2$ or $FeCl_3{\cdot}6H_2O$ (1 mmol, Sigma-Aldrich) was dissolved with respect to the desired molar ratio to the $NiCl_2$ precursor solution. After 30 minutes, the cobalt or iron precursor solution (10 mL) was added to the nickel precursor solution by a syringe with vigorous stirring accordingly. The reducing solution was added and the precipitate was collected, washed and dried to obtain final ternary metal boride black powder. During washing, the precipitates were always covered with liquid to avoid direct contact with air. For amorphous quaternary metal boride optimization, the metal precursor solution was prepared and mixed in the molar ratio: 1 : 1 : 1, 1 : 1 : 2.3, 1 : 1 : 4.6, 1 : 1 : 9.0, 0.1 : 1 : 2.3, 1 : 0.1 : 2.3 for Fe–Co–Ni–B, Fe–Co–2.3Ni–B, Fe–Co–4.6Ni–B, Fe–Co–9.0Ni–B, 0.1Fe–Co–2.3Ni–B, and Fe–0.1Co–2.3Ni–B, respectively. The reduction of Fe^{3+} ions by sodium borohydride gives formation of both Fe and B in aqueous solution, thus it is used in ternary and quaternary to favor the iron incorporation.[4] These notations of the final products were designated according to the corresponding molar ratio of metals in the pre-catalyst solution. To extend applicability of the reduced metal ions sources, Fe^{2+} was also used for highly efficient in molar ratio of 1 : 1 : 2.3 for $FeCl_2{\cdot}4H_2O$, $CoCl_2$, and $NiCl_2$. The conditions were maintained until the end of the stated period and the products were collected for further analysis without any further treatment.

1.3 Synthesis of Iron-Cobalt-Nickel Alloy

The iron-cobalt-nickel alloy was synthetized by using the procedure reported by Yang, Y. *et al.*[5] during synthesis of FeCo nanoplates. The hydrazine hydrate ($NH_2–NH_2{\cdot}H_2O$) was used as reducing agent to avoid any remaining boron residue that may be remained if the sodium borohydride is used for synthetizing metal alloy. Typically, 20 mL of precursor solution (solution A) was prepared by dissolving $FeSO_4{\cdot}7H_2O$ (1 mmol, Sigma-Aldrich), $CoCl_2$ (1 mmol, Sigma-Aldrich), and $NiCl_2{\cdot}6H_20$ (2.3 mmol, Sigma-Aldrich) under argon

atmosphere, similar molar ratio for highly efficient metal boride synthesis. The reducing solution (solution B) was prepared by mixing NaOH (988 mg, Alfa Aesar) in 4 mL of NH_2–$NH_2 \cdot H_2O$ (Sigma-Aldrich). After the addition of the solution B to solution A by a syringe with continues stirring, the reaction was occurred and witnessed by black colour appearance. The mixture was maintained at 66 °C for a half-hour, and afterward the precipitates was collected by centrifugation and they were attached to magnetic stirring showing the formation of metal alloys. Similar, the products were washed with water and ethanol for three times, respectively, followed by drying at room temperature in the vacuum overnight.

2. Catalyst Characterization

The surface morphologies of the as-prepared metal boride powders were studied by field emission scanning electron microscopy (FESEM, JEOL JSM 6701F) equiped with energy dispersive X-ray spectrometry (EDS) which was used for elemental mapping, while JED 2300 EDS on JEOL JSM 6700F SEM is used for atomic composition. Furthermore, the transmission electron microscopy (TEM) images were taken from JEOL JEM 2100F at an accelerating voltage of 200 kV. Structural characterization was determined by recording the X-ray diffraction (XRD) patterns using the Cu Kα radiation (λ = 1.5414 Å) in Bragg–Brentano configuration. The surface electronic states and composition of the as-prepared powders were carried out by X-ray photoelectron spectroscopy (XPS). XPS spectra were collected by a Kratos AXIS Ultra^{DLD} instrument equipped with a monochromatic Al Kα (1486.71 eV) X-ray source and a hemispherical analyser.

3. **Electrochemical Measurement**

Electrochemical measurements of the as-prepared metal borides and commercial Ir/C catalyst (20 wt% Ir on Vulcan carbon black from Premetek Co.) for comparison were conducted in a three-electrode cell using a rotating disk electrode (RDE, PINE Research Instrumentation) with an Autolab PGSTAT302 (Eco Chemie, Netherlands) potentiostat workstation equipped with electrochemical impedance spectroscopy (EIS) at room temperature. A platinum wire and Ag/AgCl (KCl saturated) are used as the counter and reference electrodes, respectively.[6] All the electrochemical measurements were conducted in O_2-saturated alkaline 1.0 M KOH electrolyte. The electrolyte was prepared by using potassium hydroxide pellets (semiconductor grade 99.99%, Sigma-Aldrich) and ultrapure H_2O (18.2 MΩ, Millipore).

Before loading the catalyst aliquot on GC electrodes, they were polished using aqueous alumina suspension on felt polishing pads, washed and sonicated in ethanol for few minutes, and finally, rinsed with deionized water. The catalyst and the commercial Ir/C catalyst suspensions were prepared by dispersing 10 mg of catalyst in 1 mL of solution containing 0.985 mL of ethanol and 15 µL of 5 wt% Nafion solution,[7] followed by sonication for a half-hour. Then appropriate aliquot was pipetted into pre-treated GC surface (0.196 cm^2) to give a loading of 0.3 mg/cm^2, and then dried under ambient environment.

The linear polarization curves (LSV) were recorded at a sweep rate of 5 mV s^{-1} under continuous stirring of 1600 rpm to avoid accumulation of gas bubbles over the GC electrode. Prior to linear polarization curve recording, the materials were exposed to Cyclic Voltammetry (CV) along the potential window of 0.2 V to 0.8 V vs. Ag/AgCl at 100 mV s^{-1}, until a stable CV is obtained,[8] and it comes to be 10 CVs. The onset potential for trimetallic metal boride and Ir/C catalyst reported were determined based on the current density of 1 mA cm^{-2} in the recorded LSV curves.[9] All polarization curves reported in this work were corrected for *i*R drops which was measured by the EIS technique at 0.6 V potential *vs.* Ag/AgCl for all samples and commercial 20 wt% Ir/C catalyst, while at 1.6 V for two-electrode system. The stability test was carried out by recording CV profiles of 1000 cycles at 100 mV s^{-1} from 0.2 V to 0.6 V. Furthermore, the chronopotentiometric responses were measured at a fixed current density of 10 mA cm^{-2}.

The electrochemically surface area (ECSA) was measured by double layer capacitance method derived from cyclic voltammetry (CV) measured in static solution.[10] To determine the capacitance value, catalysts deposited onto glassy carbon electrode were first activated by 25 cyclic voltammetry scans and in order to observe no-faradaic region. Then 10 cyclic voltammetry scans were performed at different scan rate in a potential window where no Faradaic process occurs, at different scan rates: 16, 14, 12, 10, 8, 6, and 4 mV s^{-1}.[11] The capacitance was determined from the tenth cyclic voltammetry curve of each scan rate. After data collection the following equation: $C_{dl} = Ic/\nu$ was used for electrochemical double-layer capacitance, where C_{dl} is the double-layer capacitance (mF cm^{-2}) of the electroactive materials, *Ic* is charging current (mA cm^{-2}), and ν is scan rate (mV s^{-1}).[12] The average specific current density, j_s,[10, 13] is normalized for ECSA at η =

0.314 V. It is calculated by dividing the current density per geometric area at a given overpotential, j_g, by the roughness factor of the surface as shown in equation 2:

$$j_s = j_g / \mathrm{RF} \quad (2)$$

The average current density per geometric area at η = 0.314 V which is the overpotential required to deliver a current density of 10 m cm^{-2} for the as-synthetized nickel boride, j_g, η = 0.314 V. The choice of η = 0.314 V is based on previously reported device models that suggest a 10% efficient solar water-splitting device should operate at 10 mA cm^{-2}.[10] The ECSA of a catalyst sample is calculated from the double layer capacitance according to equation 3:

$$\mathrm{ECSA} = C_{dl}/C_s \quad (3)$$

where C_s is the specific capacitance of the sample or the capacitance of an atomically smooth planar surface of the material per unit area under identical electrolyte conditions. The roughness factor (RF) is calculated by taking the estimated ECSA and dividing by the geometric area of the electrode, 0.196 cm^2.[10] All measured potentials reported in this paper were converted from *vs.* Ag/AgCl to *vs.* RHE by adding a value of 0.197 + 0.059 × pH. In addition, all reported current density was normalized to the geometric surface area. The overpotential was calculated as follows:

$\eta = E\ (vs.\ RHE) - 1.23$,

considering O_2/H_2O equilibrium at 1.23 V *vs.* RHE.

3.1 Complete water electrolysis

To study the functionality of this material toward water splitting, overall water electrolysis was performed in a two-electrode system where the modified carbon fiber paper (CFP) with the as-prepared material and 50% Pt carbon catalyst (50% Pt/C - GasHub Technology) used as anodic and cathodic electrode, respectively. Furthermore, the similar study was investigated by using modified carbon cloth (CC) as a sole electrode active material. The ink of amorphous quaternary Fe–Co–2.3Ni–B powder as well as 50% Pt/C prepared with similar procedure for three-electrode catalyst were loaded into the pieces of CC and/or CFB until a final loading of 4.0 mg/cm^2 is reached, respectively. Afterwards, once the electrodes were completely dried at ambient temperature, they were mounted on both electrodes and dipped in an open cell containing

1.0 M KOH electrolyte solution. The modified electrodes were moisturized for 20 minutes, and then activated by recording 10 continuous cyclic voltammograms between 1 V and 2.0 V at 50 mV s^{-1}. Then polarization curve was performed across a potential window from 1.2 or 0.8 V to 2.2 V when Fe–Co–2.3Ni–B catalyst is used on both anode and cathode and when the Pt/C cathode is used, respectively, at a scan rate of 5 mV s^{-1}. The long-term stability was also examined using a similar procedure described for OER study.

Table S1: EDS Elemental atomic percentages for amorphous quaternary metal boride catalyst.

Element	Elemental Atomic %[a]	Elemental Atomic %[b]
B	8.4	2.4
O	~[c]	3.7
Fe	10.4	9.4
Co	23.8	25.3
Ni	57.4	59.2
Total	100	100

[a] Elemental atomic % before electrochemical test. [b] Elemental atomic % after electrochemical test. [c] Negligible oxygen atomic percentage was omitted for the elemental atomic % calculation of the as-synthesized due to the reason described in discussion section.

Table S2: Electrochemical results of the amorphous metal-boron nanomaterial and commercial 20 wt% Ir/C catalysts in 1 M KOH electrolyte at room temperature.

Catalyst (Supported on GC otherwise stated)	Potential (V)[a] at $J_{10\ \&\ 20}$ (mA cm^{-2})		Tafel slope (mV dec^{-1})
	10	20	
Ir/C	1.547	1.578	53
Fe–Co–2.3Ni–B	1.504	1.516	38
0.1Fe–Co–2.3Ni–B	1.537	1.555	54
Fe–0.1Co–2.3Ni–B	1.536	1.554	67
Fe–Co–Ni–B	1.514	1.531	49
Fe–Co–4.6Ni–B	1.521	1.542	59
Fe–Co–9.0Ni–B	1.522	1.545	63
Fe–2.3Ni–B	1.524	1.542	53
Co–2.3Ni–B	1.547	1.561	49
Co–B	1.552	1.574	72
Ni–B	1.544	1.561	52
Fe–B	1.595	1.622	72
Mixture of M–B [b]	1.537	1.558	57

[a] reversible hydrogen electrode, [b] mixture of cobalt boride, iron boride and nickel boride in the mass ratio 1 : 1 : 2.3, Fe–B : Co–B : Ni–B powders.

Table S3. OER and overall water splitting (OWS) activities of the amorphous quaternary metal boride catalyst and reported Fe-, Co-, and Ni-based catalysts.

Catalyst	Electrolyte	Reference Electrode	Scanning rate (mV/s)	Loading (mg cm^{-2})	Tafel slope (mV dec^{-1})	OER Potential @10 mA cm^{-2}	OWS Potential @10 mA cm^{-2}	References
Fe-Co-2.3Ni-B	**1 M KOH**	**Ag/AgCl**	**5**	**0.3**	**38**	**1.50**	**1.52@20,[a] 1.66[b]**	**This work**
Fe-Co-2.3Ni Alloy				**0.3**	**45**	**1.55**	-	**This work**
$Ni_{30}Fe_7Co_{20}Ce_{43}O_X$	1 M NaOH	Hg/HgO	**10**	-[c]	70	1.54	-[c]	Energy Environ. Sci. **2014**, 7, 682
NiCoFe-LDH [d]	0.1 M KOH	Hg/HgCl	1	0.12	~120	~1.70	-[c]	Adv. Energy Mater. **2015**, 5, 1500245
O-NiCoFe-LDH				0.12	~93	~1.57		
Ni-$Fe_{0.52}$ LDH	1 M KOH	Hg/HgO	-[c]	0.14	97	1.57	-[c]	Dalton Trans. **2015**, **44**, 11592
NiSe/NF	1 M KOH	Ag/AgCl	2	2.8	64	1.50 @20	1.63	Angew. Chem. Int. Ed. **2015**, 54, 9351
$NiCo_2S_4$NA/CC	1 M KOH	Hg/HgCl	2	0.43	89	1.51 @20	1.68	Nanoscale **2015**, 7, 15122.
$NiCo_2O_4$NA/CC				0.43	90	1.60 @20	-[c]	
FeP/CC	1 M KOH	Ag/AgCl	5	1.6	43	1.52	1.69	Chem. Eur. J. **2015**, 21, 18062
Ni_2P	1 M KOH.	Ag/AgCl	5	5.0 [e]	47	1.52	1.63	Energy Environ. Sci. **2015**, 8
Co-P films	1 M KOH	Ag/AgCl	2	3.7	47	1.57	1.64	Angew. Chem. Int. Ed. **2015**, 54, 6251
hollow NCNTFs	1 M KOH	Ag/AgCl	5	0.2	93	1.60	-[c]	Nature Energy **2016**, 1, 15006
Ni-B/NF	1 M KOH	Hg/HgCl	2	12.3	76	1.59 @100	1.69 @15	Nanotechnology **2016**, 27, 12LT01.

Co_2B-500	0.1 M KOH	Ag/AgCl	10	0.21	45	1.61	1.81[f)]	Adv. Energy Mater. **2016**, 6, 1502313
Co-Bi NS/G	1 M KOH	Ag/AgCl	5	0.285	53	1.52	-[c)]	Angew. Chem. Int. Ed. 2016, 55, 2488
Ni_3FeN-NPs	1 M KOH	Ag/AgCl	5	0.35	46	1.51	-[c)]	Adv. Energy Mater. **2016**, 6, 1502585.
Ni_3FeN-bulk				0.35	67	1.54	-[c)]	
$NiCo_2O_4$	1 M NaOH	Hg/HgCl	0.1	0.6	53	1.52	1.65	Angew. Chem. Int. Ed. **2016**, 55, 6290
EG/$Co_{0.85}Se$ /NiFe-LDH	1 M KOH	Ag/AgCl	1	4.0	57	1.50 @150	1.67,	Energy Environ. Sci. **2016**, 9, 478
Ir/C // Pt/C				4.0			1.64	
NiFe/Co_3O_4/NF	1 M KOH	Ag/AgCl	5	-[c)]	45	1.50 @1.0		Adv. Funct. Mater. **2016**, 26, 3515
NiFe/$NiCo_2O_4$/NF				-[c)]	39	1.47 @1.0	1.67	
MoO_x/Ni_3S_2/NF	1 M KOH	Hg/HgO	-[c)]	12	50	1.37	~1.45	Adv. Funct. Mater. **2016**, 26, 4839
$CoSn(OH)_6$ nanocubes	1 M KOH	Ag/AgCl	1	~0.3		1.50		Energy Environ. Sci., **2016**, **9**, 473
MoS_2/Ni_3S_2	1 M KOH	Hg/HgO	1	7.0	88	1.45	1.56	Angew. Chem. Int. Ed. **2016**, 55, 6702.
$NiO/NiFe_2O_4$	1 M KOH	Hg/HgCl	5	-[c)]	58	1.53	-[c)]	**J**. Mater. Chem. A**, 2017**,**5**, 4320
PPy/FeTCPP/Co	1 M KOH	Hg/HgCl	10	0.3	61	1.57	-[c)]	Adv. Funct. Mater. **2017**, 27, 1606497
$Fe_{1.1}Mn_{0.9}P$	1 M KOH	Ag/AgCl	10	0.284	39	1.58	-[c)]	Chem. Mater. **2017**, 29, 3048
H_2O-Plasma Exfoliated LDHs	1 M KOH	Hg/HgCl	5	0.204	36	1.51	-[c)]	*Adv. Mater.* **2017**, 1701546
Activated Mn-Co oxyphosphide	1 M KOH	Ag/AgCl	10	0.25	52	1.55	-[c)]	Angew. Chem. Int. Ed. **2017**, 56, 2386
Mn-Co oxyphosphide					60	1.60		
Mn-Co oxide					66	1.65		

NiCoP/C nanoboxes NiCoP nanoboxes Ni–Co LDH nanoboxes	1 M KOH	Ag/AgCl	10	0.25	96 115 135	1.56 1.60 1.65	-[c]	Angew. Chem. Int. Ed. **2017**, 56, 3897– 3900
CoFe LDHs-Ar	1 M KOH	Hg/HgCl	5	0.204	38	1.50	-[c]	Angew. Chem. Int. Ed. 2017, 56, 5867-5871
Ni-Bi@NB	1 M KOH	Hg/HgO	5	0.3	52	1.53	-[c]	Angew. Chem. Int. Ed. 2017, 56, 6572 –6577

[a] Two-electrode system whereby the as-prepared material is used as anodic material while Pt/C as the cathodic electrode on CFP, and [b] when is used as anodic and cathodic electrode active material on CC with a loading of 4.0 mg cm^{-2}. [c] Data not available in literature, [d] Catalyst mixed with carbon black (5.0 mg of catalyst, 2.0 mg of carbon black) and measurements in 0.1 M KOH electrolyte at 1.0 mV s^{-1}, [e] Loading for OER is 0.14 mg cm^{-2}. [f] Electrolyte concentration of 0.1 M KOH and 3 M KOH, for OER and overall water splitting with with a loading of 5.0 mg cm^{-2} approximately, respectively.

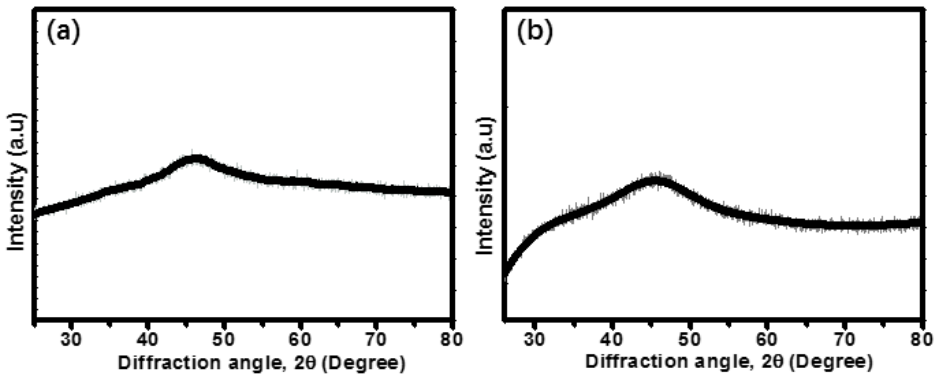

Figure S1. a) XRD patterns of amorphous ternary Fe–2.3Ni–B, and (b) Co–2.3Ni–B powders.

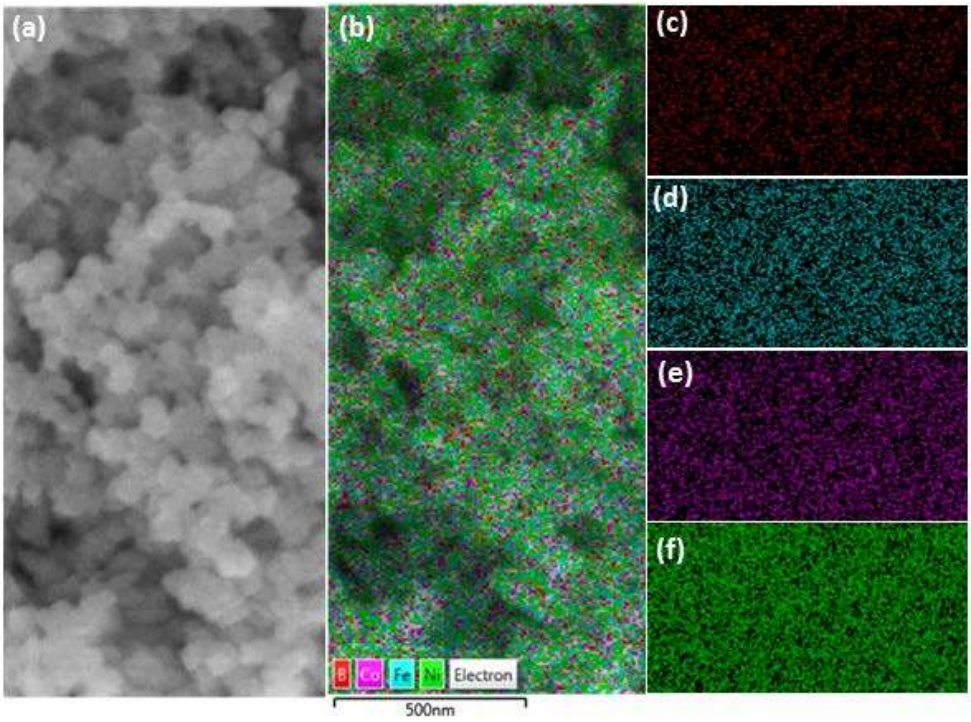

Figure S2. a) SEM image of the amorphous quaternary Fe–Co-2.3Ni–B powders, and (b) corresponding EDS layered image. Corresponding EDS elemental mappings; B Kα1 (c), Fe Kα1 (d), Co Kα1 (e), and Ni Kα1 (f).

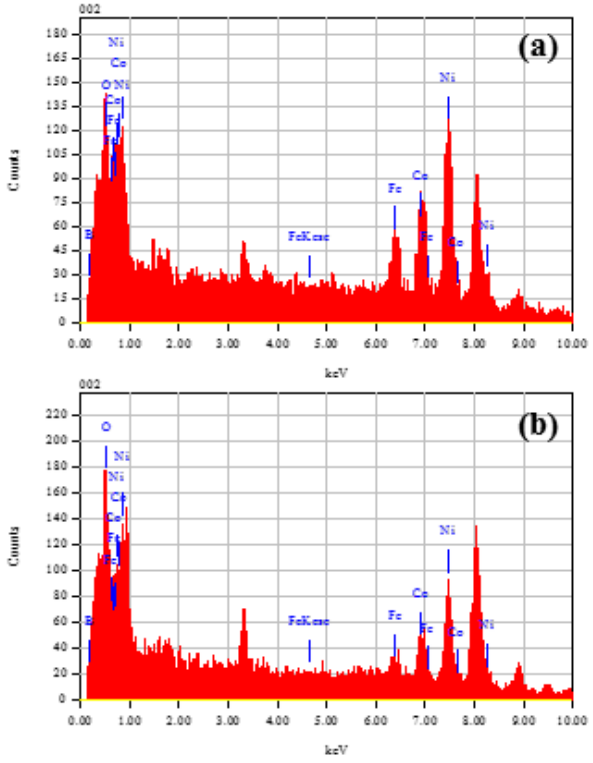

Figure S3. a) EDS pattern for amorphous quaternary Fe–Co–2.3Ni–B before, and (b) after stability test.

Notes: The peak at ~ 8.3 keV arises from (the Cu peaks arise from the Cu mesh).

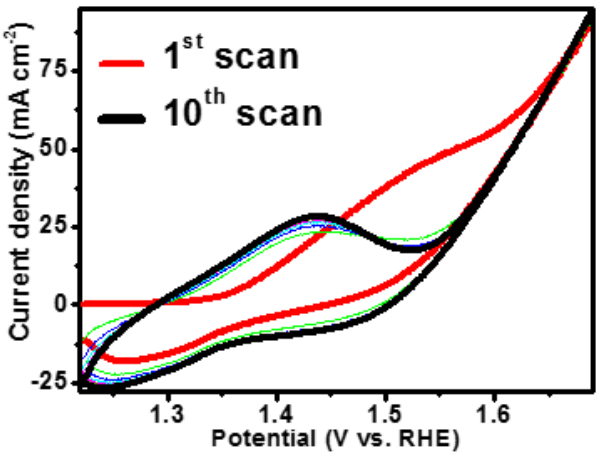

Figure S4. Activation curves of the as-synthesized amorphous Fe–Co–2.3Ni–B catalyst at 100 mV s^{-1} scanning rate in alkaline electrolyte at ambient temperature.

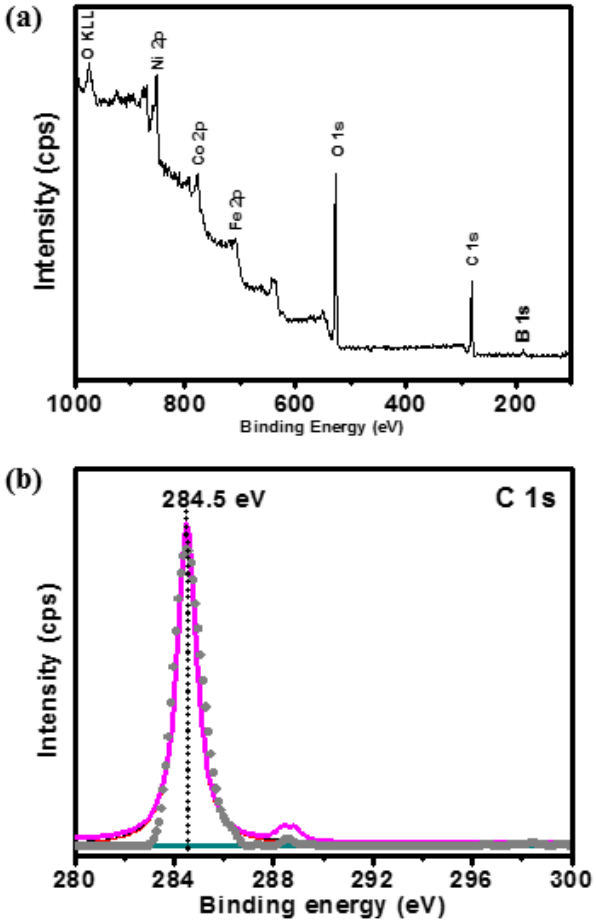

Figure S5. a) XPS survey spectrum for the amorphous quaternary Fe–Co–2.3Ni–B powders, and (b) High-resolution XPS spectrum of C 1s.

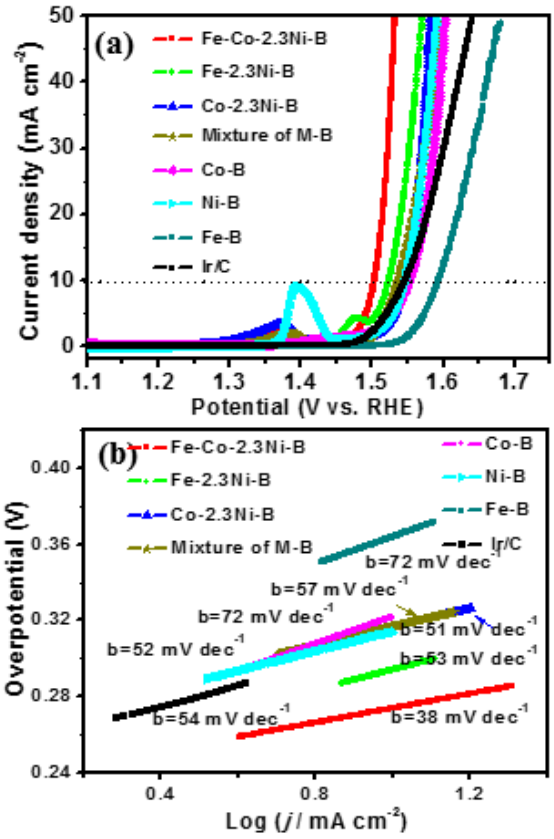

Figure S6. a) *i*R-corrected LSV curves polarization curves, and (b) corresponding Tafel slopes of different catalysts in 1 M KOH electrolyte at room temperature. The horizontal-dashed line at a j_{geo} of 10 mA cm^{-2} in the current density vs. potential plot is the current density expected for a 10% efficient solar water-splitting device.[14]

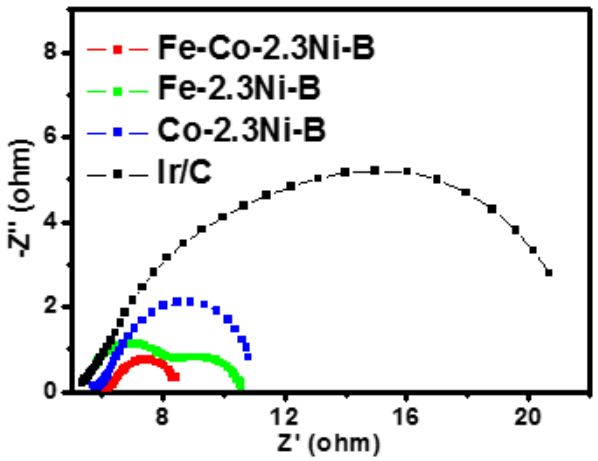

Figure S7. Nyquist plots of the amorphous quaternary Fe–Co–2.3Ni–B, Fe–2.3Ni–B, Co–2.3Ni–B, and commercial 20 wt% Ir/C catalyst. The electrochemical impedance spectroscopies (EIS) measured at 0.6 V *vs.* Ag/AgCl at room temperature in 1 M KOH electrolyte. Notes: Z' is the real part and -Z'' is the imaginary part. The high-frequency intercept of the semicircle on the real axis is assigned to the ohmic series resistance (Rs). Rs for Fe–Co–2.3Ni–B, Fe–2.3Ni–B, Co–2.3Ni–B, and Ir/C are 6.0, 5.2, 5.6, 5.2 Ohm respectively.

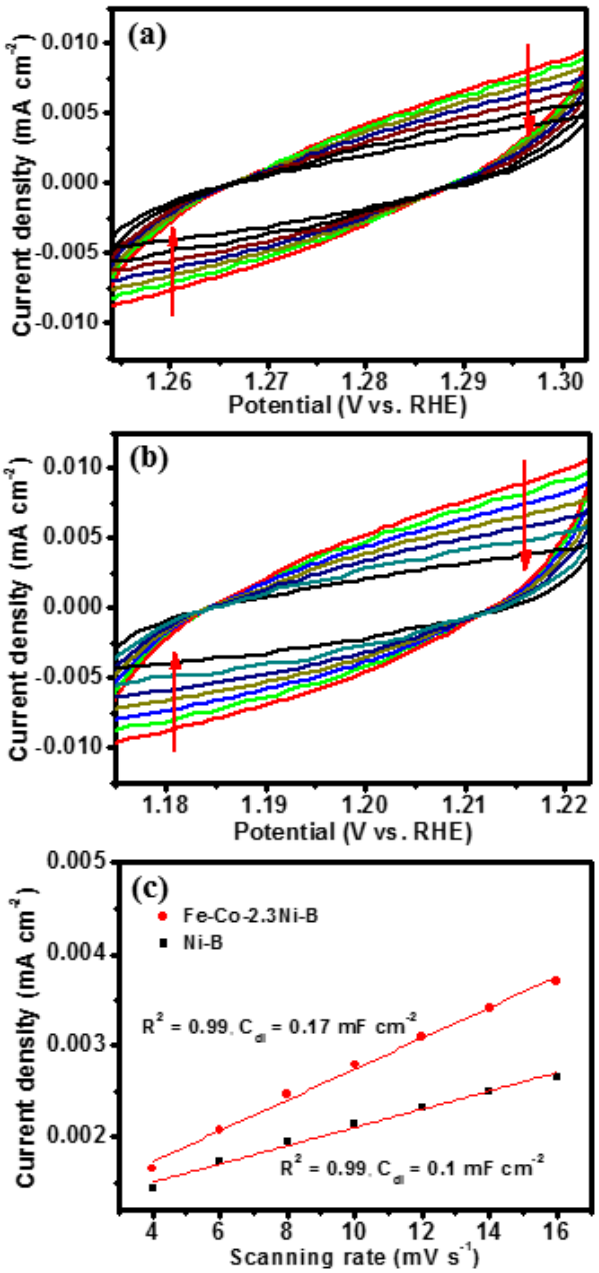

Figure S8. a) Cyclic voltammograms in the double layer region at scan rate of 16, 14, 12, 10, 8, 6, 4 mV/s (along the arrow direction) of Ni–B nanoparticle, and (b) Fe–Co–2.3Ni–B nanoparticle. c) Current density as a function of scan rate derived from (a) and (b).

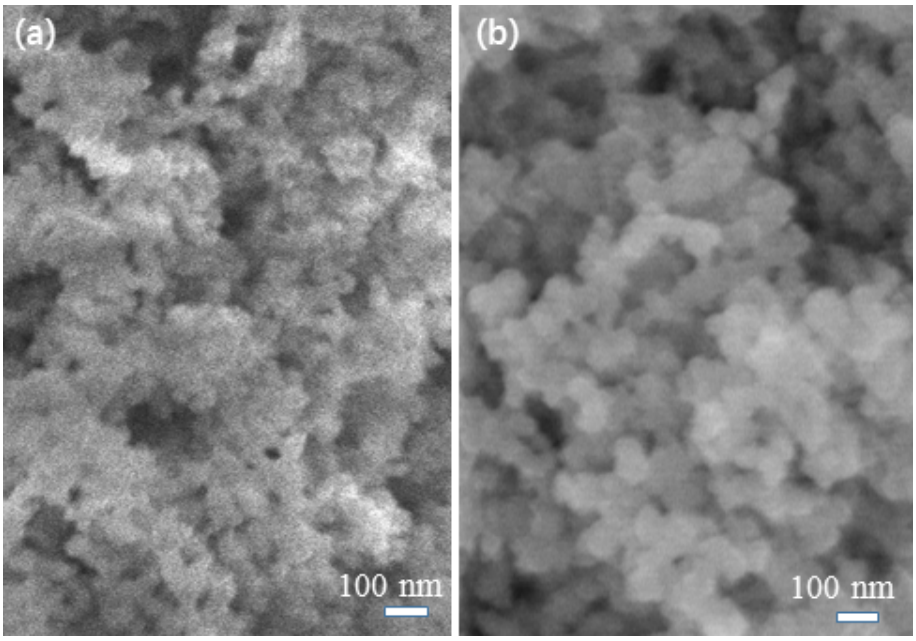

Figure S9. a) SEM image for Ni–B, and (b) amorphous trimetallic Fe–Co–2.3Ni–B nanoparticles.

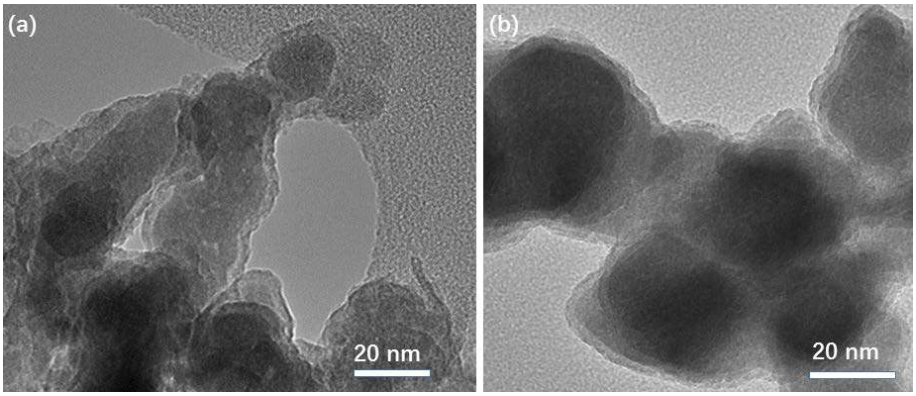

Figure S10. a) TEM image for Ni–B, and (b) amorphous trimetallic Fe–Co–2.3Ni–B nanoparticles.

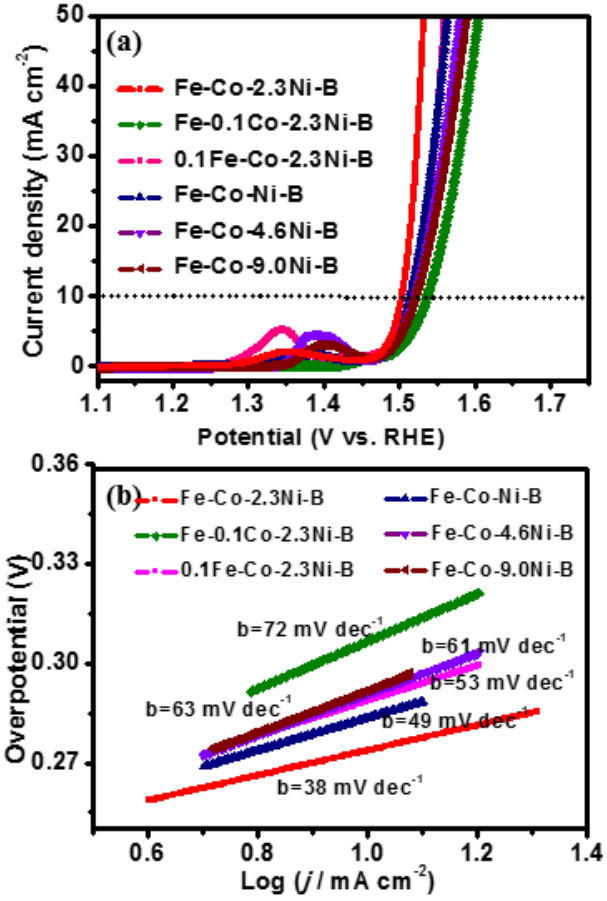

Figure S11. a) *i*R-corrected LSV curves polarization curves, and (b) corresponding Tafel slopes of amorphous trimetallic metal boride catalysts in 1 M KOH electrolyte at room temperature. The horizontal-dashed line at a j_{geo} of 10 mA cm^{-2} in the current density vs. potential plot is the current density expected for a 10% efficient solar water-splitting device.[14]

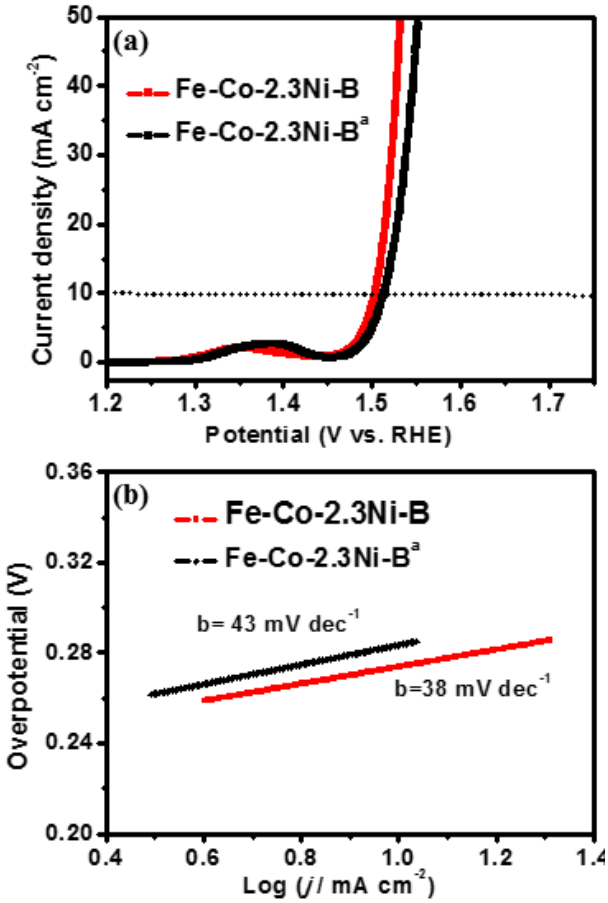

Figure S12. a) *i*R-corrected polarisation curves, and (b) corresponding Tafel slopes for amorphous Fe–Co–2.3Ni–B and Fe–Co–2.3Ni–B[a] ([a]prepared by using Fe^{2+} ion as iron source) recorded in 1 M KOH electrolyte at the same conditions. The horizontal-dashed line at a j_{geo} of 10 mA cm^{-2} in the current density vs. potential plot is the current density expected for a 10% efficient solar water-splitting device.[14]

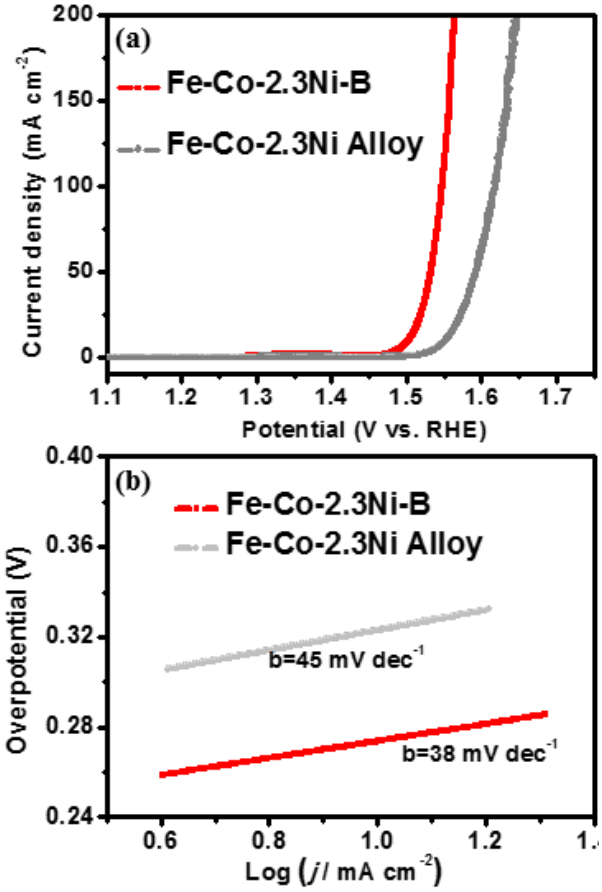

Figure S13. a) *i*R-corrected polarisation curves, and (b) corresponding Tafel slopes for amorphous Fe–Co–2.3Ni–B and Fe–Co–2.3Ni recorded in 1 M KOH electrolyte at the same conditions. The horizontal-dashed line at a j_{geo} of 10 mA cm^{-2} in the current density vs. potential plot is the current density expected for a 10% efficient solar water-splitting device.[14]

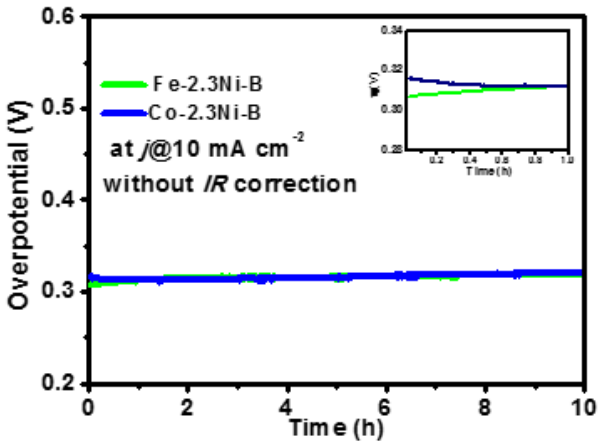

Figure S14. Galvanostatic long-term durability test at a constant current density of 10 mA cm^{-2} over 10 h period of the as-prepared ternary Fe–2.3Ni–B and Co–2.3Ni–B catalyst at room temperature in 1.0 KOH electrolyte.

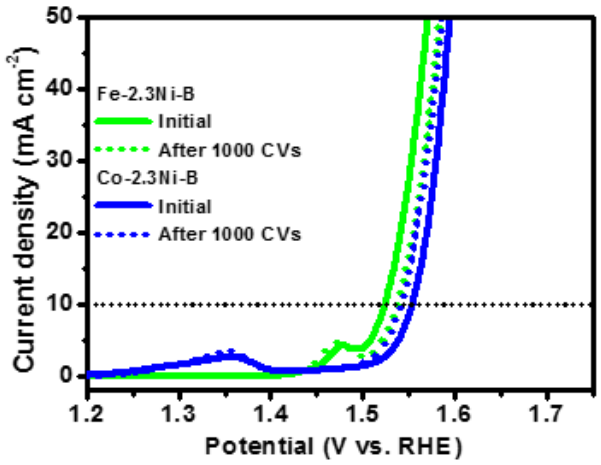

Figure S15. The electrochemical stability test by CV of the as-prepared ternary Fe–2.3Ni–B and Co–2.3Ni–B catalysts at room temperature in 1.0 KOH electrolyte: *i*R-corrected polarisation curves recorded before and after 1000 CVs in the potential window of 0.2 V to 0.6 *vs.* Ag/AgCl at a scan rate of 100 mV s^{-1}.

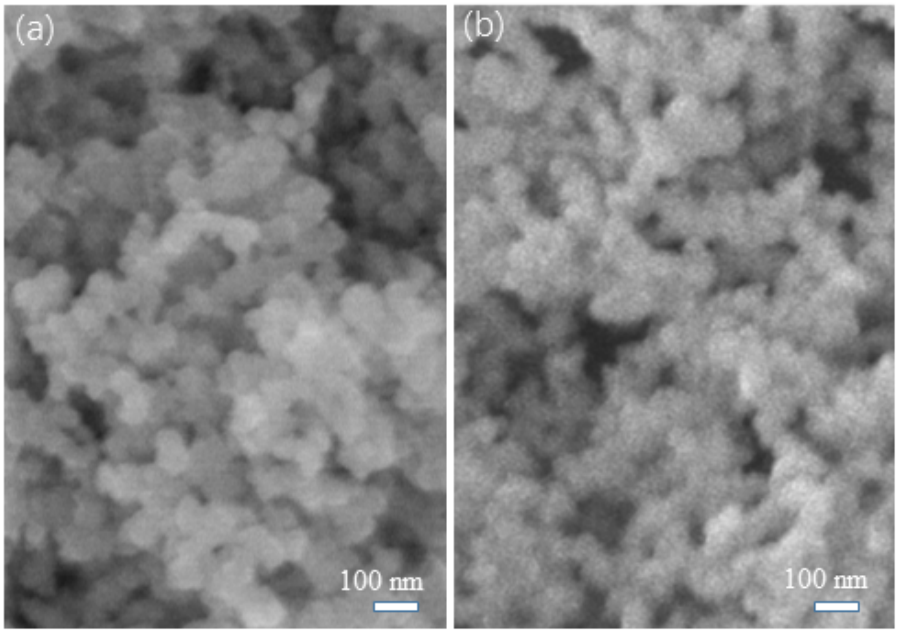

Figure S16. a) SEM image for amorphous trimetallic Fe–Co–2.3Ni–B nanoparticles before, and (b) after galvanostatic long-term durability test. The material was washed with water and ethanol several times to remove electrolyte.

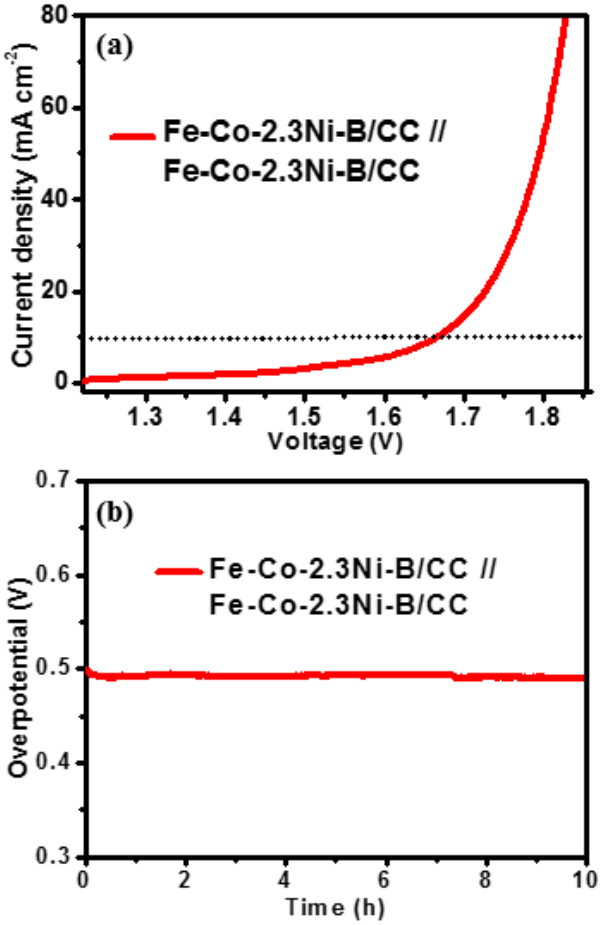

Figure S17. Two-electrode alkaline electrolyzer with carbon cloth modified by the as-prepared quaternary amorphous metal boride as both the anode and cathode; (a) Current-potential response measured in 1 M KOH electrolyte, and (b) galvanostatic electrolysis at 10 mA cm^{-2} over 10 hours. The horizontal-dashed line at a j_{geo} of 10 mA cm^{-2} in the current density vs. voltage plot is the current density expected for a 10% efficient solar water-splitting device.[14]

References

[1] a) B. Ganem, J. O. Osby, *Chem. Rev.* **1986**, *86*, 763; b) J. Masa, P. Weide, D. Peeters, I. Sinev, W. Xia, Z. Sun, C. Somsen, M. Muhler, W. Schuhmann, *Adv. Energy Mater.* **2016**, *6*, 1502313.

[2] G. M. Arzac, T. C. Rojas, A. Fernandez, A. Fernández, *ChemCatChem* **2011**, *3*, 1305.

[3] G. N. Glavee, K. J. Klabunde, C. M. Sorensen, G. C. Hadjapanayis, *Langmuir* **1992**, *8*, 771.

[4] G. N. Glavee, K. J. Klabunde, C. M. Sorensen, G. C. Hadjipanayis, *Inorg Chem* **1995**, *34*, 28.

[5] Y. Yang, C. Xu, Y. Xia, T. Wang, F. Li, *J. Alloys Compd.* **2010**, *493*, 549.

[6] Y. Yan, B. Zhao, S. C. Yi, X. Wang, *J. Mat. Chem. A* **2016**, *4*, 13005.

[7] X. Jia, Y. Zhao, G. Chen, L. Shang, R. Shi, X. Kang, G. I. N. Waterhouse, L.-Z. Wu, C.-H. Tung, T. Zhang, *Adv. Energy Mater.* **2016**, *6*, 1502585.

[8] Y. Hou, M. R. Lohe, J. Zhang, S. Liu, X. Zhuang, X. Feng, *Energy Environ. Sci.* **2016**, *9*, 478.

[9] a) Y. Yan, B. Y. Xia, X. Ge, Z. Liu, A. Fisher, X. Wang, *Chem. Eur. J.* **2015**, *21*, 18062; b) L.-J. Zhou, X. Huang, H. Chen, P. Jin, G.-D. Li, X. Zou, *Dalton Trans.* **2015**, *44*, 11592.

[10] C. C. L. McCrory, S. Jung, J. C. Peters, T. F. Jaramillo, *J. Am. Chem. Soc.* **2013**, *135*, 16977.

[11] R. Chen, H.-Y. Wang, J. Miao, H. Yang, B. Liu, *Nano Energy* **2015**, *11*, 333.

[12] P. He, X. Y. Yu, X. W. Lou, *Angew. Chem. Int. Ed.* **2017**, *56*, 3897.

[13] C. C. L. McCrory, S. Jung, I. M. Ferrer, S. M. Chatman, J. C. Peters, T. F. Jaramillo, *J. Am. Chem. Soc.* **2015**, *137*, 4347.

[14] M. G. Walter, E. L. Warren, J. R. McKone, S. W. Boettcher, Q. X. Mi, E. A. Santori, N. S. Lewis, *Chem. Rev.* **2010**, *110*, 6446.